Creating Conjugated C−C Bonds between Commercial Carbon Electrode and Molecular Catalyst for Oxygen Reduction to Hydrogen Peroxide

Biemolt, Jasper; Meeus, Eva J.; de Zwart, Felix J.; de Graaf, Jeen; Laan, Petrus C.M.; de Bruin, Bas; Burdyny, Thomas; Rothenberg, Gadi; Yan, Ning

DOI
10.1002/cssc.202300841

Publication date
2023

Document Version
Final published version

Published in
ChemSusChem

Citation (APA)
Biemolt, J., Meeus, E. J., de Zwart, F. J., de Graaf, J., Laan, P. C. M., de Bruin, B., Burdyny, T., Rothenberg, G., & Yan, N. (2023). Creating Conjugated C−C Bonds between Commercial Carbon Electrode and Molecular Catalyst for Oxygen Reduction to Hydrogen Peroxide. *ChemSusChem*, *16*(18), Article e202300841. https://doi.org/10.1002/cssc.202300841

ChemSusChem

Research Article
doi.org/10.1002/cssc.202300841

Chemistry Europe
European Chemical Societies Publishing

www.chemsuschem.org

VIP *Very Important Paper*

Creating Conjugated C–C Bonds between Commercial Carbon Electrode and Molecular Catalyst for Oxygen Reduction to Hydrogen Peroxide

Jasper Biemolt,[a, b] Eva J. Meeus,[a] Felix J. de Zwart,[a] Jeen de Graaf,[a] Petrus C. M. Laan,[a] Bas de Bruin,[a] Thomas Burdyny,[b] Gadi Rothenberg,*[a] and Ning Yan*[a, c]

Immobilizing molecular catalysts on electrodes is vital for electrochemical applications. However, creating robust electrode-catalyst interactions while maintaining good catalytic performance and rapid electron transfer is challenging. Here, without introducing any foreign elements, we show a bottom-up synthetic approach of constructing the conjugated C–C bond between the commercial Vulcan carbon electrode and an organometallic catalyst. Characterization results from FTIR, XPS, aberration-corrected TEM and EPR confirmed the successful and uniform heterogenization of the complex. The synthesized Vulcan-LN_4–Co catalyst is highly active and selective in the oxygen reduction reaction in neutral media, showing an 80% hydrogen peroxide selectivity and a 0.72 V (vs. RHE) onset potential which significantly outperformed the homogenous counterpart. Based on single-crystal XRD and NMR data, we built a model for density functional theory calculations which showed a nearly optimal binding energy for the *OOH intermediate. Our results show that the direct conjugated C–C bonding is an effective approach for heterogenizing molecular catalysts on carbon, opening new opportunities for employing molecular catalysts in electrochemical applications.

Introduction

The design, modification and understanding of catalytic active sites has been a central research focus in catalysis to produce chemical species at high efficiencies and production rates. Compared with heterogeneous catalysts,[1–4] homogeneous counterparts often enjoy well-defined active sites,[5,6] yet suffering from difficult product separation. Therefore, heterogenized molecular catalysts come to the spotlight, while bringing new factors affecting the performance of the active site.[7–9] For instance, the proximity of a solid support to an organometallic complex yields confinement effects which affect the product selectivities;[10,11] moreover, the electronic interactions between supports and molecular catalysts can alter reaction pathways.[12] Such heterogenization strategy is frequently used in electrocatalysis where rapid electron transfer between the active site and the electrode is a must.[13–17] For example, the supported cobalt phthalocyanine molecules enabled electrochemical reduction of CO_2 toward CO with high rate and selectivity.[18] We also reported the doped carbon anchored Fe phthalocyanine catalyst which offered excellent oxygen reduction activity.[19] In many cases, the immobilized complexes showed distinct redox and catalytic properties due to the unique interaction between the support and the molecule.[20–25] Understanding the interfacial effects together with developing a robust interface is thus important.

Nevertheless, the immobilization strategies used in many heterogenized systems are based on surface adsorption, electrostatic/hydrophobic interactions and self-assembly using ligands containing foreign elements (e.g., thiols and dithiols). On one hand, the weak interaction based on the Van der Waals force or π-π interaction might undermine the stability of the system,[26,27] causing leaching of the molecular catalysts. On the other hand, the introduced ligands with foreign elements might complicate the interface, changing the catalytic behaviours of the active centre (e.g., via second coordination sphere effects) and slowing down the electron transfer rate.[28] In this context, we envisage that creating a strong yet "clean and simple" interaction between the support and the molecular catalyst will make the most of active sites from the complexes, while empowering us to better understand the interfacial effect.

[a] Dr. J. Biemolt, E. J. Meeus, F. J. de Zwart, J. de Graaf, P. C. M. Laan, Prof. Dr. B. de Bruin, Prof. Dr. G. Rothenberg, Prof. Dr. N. Yan
Van't Hoff Institute for Molecular Sciences (HIMS)
University of Amsterdam
Science Park 904, 1098XH Amsterdam (The Netherlands)
,
E-mail: g.rothenberg@uva.nl
n.yan@uva.nl

[b] Dr. J. Biemolt, Dr. T. Burdyny
Materials for Energy Conversion and Storage (MECS), Department of Chemical Engineering, Faculty of Applied Sciences
Delft University of Technology
2629 HZ Delft (The Netherlands)

[c] Prof. Dr. N. Yan
School of Physics and Technology
Wuhan University
430072, Wuhan (P. R. China)
E-mail: ning.yan@whu.edu.cn

Supporting information for this article is available on the WWW under https://doi.org/10.1002/cssc.202300841

A C–C conjugated system is ideal to build such interface as the active site is now located within the conductive graphite matrix which is a common electrode material. This configuration is similar to the active sites in doped carbons, allowing higher turnover frequency and inner-sphere electron transfer (ET) to the active site.[29–34] Yet, ensuring sufficient electronic conductivity is problematic. Here we use commercial carbon (Vulcan XC-72R) as the model and report the anchoring of a molecular Co(bpb) complex on the surface via a direct conjugated C–C bond. Using a bottom-up synthetic approach, an optimal electrode-active site interaction is created without introducing foreign elements. X-ray photoelectron spectroscopy (XPS) and electron paramagnetic resonance spectroscopy (EPR) showed a strong interaction between the cobalt centre and electrode, with a induced change in the cobalt oxidation state. The anchored complex showed no redox activity in non-coordinating electrolyte, as ionic transfer through the double layer does not occur. In the oxygen reduction reaction (ORR) in neutral media (where the reaction is more sluggish as both hydronium cations and hydroxide anions are much lower than those at extreme pH values), the anchored catalyst efficiently and selectively catalysed the formation of H_2O_2, showing an onset potential of 0.72 V vs. RHE and a H_2O_2 selectivity of 80%. Our density functional theory (DFT) calculations showed that the H_2O_2 selectivity originates from the close to optimal *OOH binding ($\triangle G_{*OOH} = 4.34$ eV) and less ideal *OH binding ($\triangle G_{*OH} =$ 1.12 eV). The direct conjugated C–C bond is an effective approach of immobilizing molecular catalysts on carbon without causing negative effects. It opens new avenues for the practical applications of molecular catalysts in electrochemical devices.

Results and Discussion

Synthesis and anchoring

Metal complexes with N_4-type ligands are often stable and electrocatalytically active. Here we used the 1,2-bis(pyridine-2-carboxamido)benzenate (bpb) ligand as the organic part of the anchored organo-metallic complex. To ensure a strong electrode/active site interaction, we used diazonium grafting to form a direct conjugated bond between the organometallic complex and surface (Scheme 1).[35,36] As grafting requires harsh conditions, which can leach the metal, we initially grafted the ligand and subsequently introduced the cobalt centre. Diazonium grafting requires an amine group on the backbone of the ligand (bpb-NH_2) for the diazonium formation. To simplify the synthesis, we coupled 4-nitro-1,2-phenylenediamine and picolinic acid to form bpb-NO_2, which after reduction yields bpb-NH_2 (FT-IR, ^{1}H-NMR and full experimental procedures are provided in the supporting information). The diazonium bpb analogue (bpb-N_2) was generated using sodium nitrite and hydrochloric acid, and directly grafted onto Vulcan XC-72R (herein: Vulcan-LN_4). The anchored organometallic Co(bpb)OAc was prepared by adding $Co(OAc)_2.4H_2O$ (sample dubbed Vulcan-LN_4–Co). For the homogeneous equivalent [Co-(bpb)OAc], 1,2-bis(pyridine-2-carboxamido)benzenate (bpb) was prepared from o-phenylenediamine and picolinic acid with triphenylphosphite, with Co(bpb)OAc forming instantaneously after adding $Co(OAc)_2.4H_2O$.

The successful grafting of the bpb ligand on the Vulcan surface was first evaluated using thermogravimetric analysis (TGA) under inert conditions (Figure 1a). Vulcan carbon retains its mass up to 600 °C, while Vulcan-LN_4 has an initial gradual mass loss up to ≈370 °C and a rapid loss between 370–450 °C. The first mass loss is related to the loss of solvent or other adsorbed species, while the second pertains to the decomposition of anchored ligand. An exact ligand mass loading

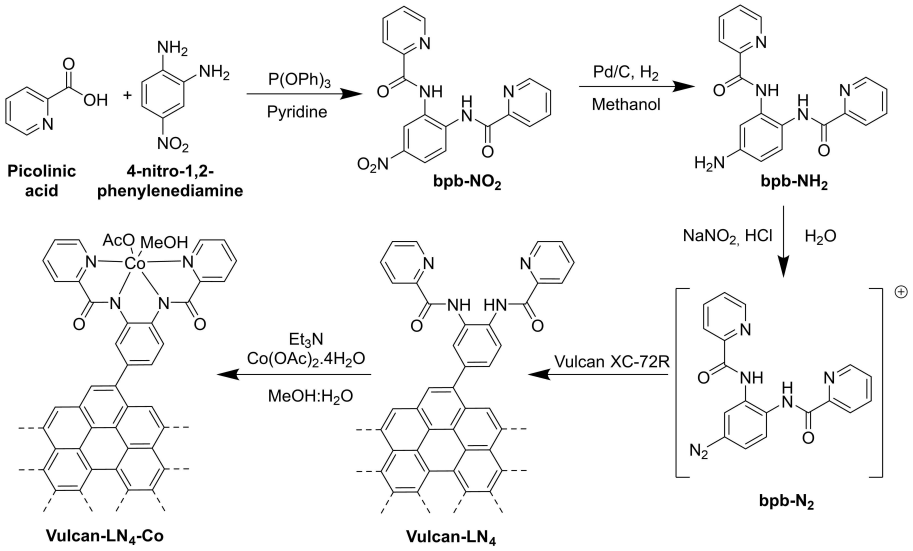

Scheme 1. The synthetic strategy used in this research for anchoring the molecular complex to the carbon support.

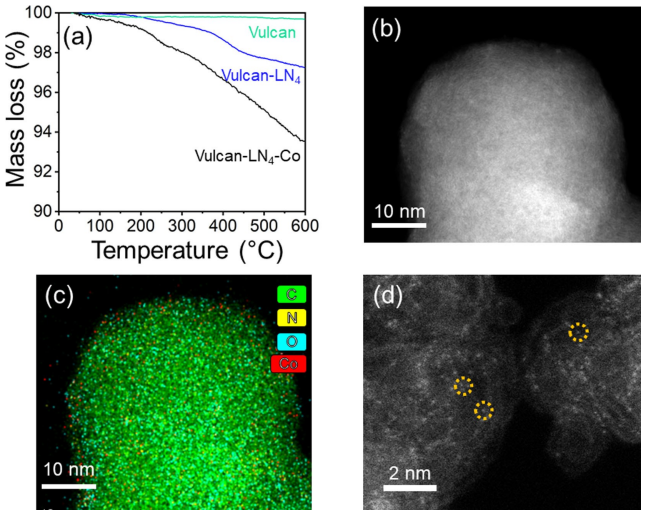

Figure 1. (a) Thermogravimetric analysis of Vulcan, Vulcan-LN_4 and Vulcan-LN_4–Co; (b) HAADF-STEM image, (c) EDX elemental mapping and (d) high resolution image of Vulcan-LN_4–Co, the circled white dots are examples of Co single atoms in the LN_4–Co complex.

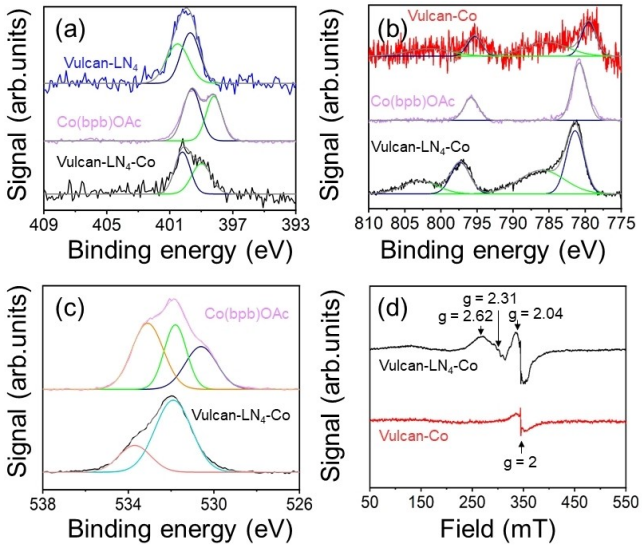

Figure 2. (a) N 1s XP spectra of Vulcan-LN_4, Vulcan-LN_4–Co and Co(bpb)OAc, (b) Co 2p XP spectra of Vulcan-LN_4–Co, Vulcan-Co, and Co(bpb)OAc, (c) O 1s XP spectra of Vulcan-LN_4–Co and Co(bpb)Oac and (d) EPR spectra of Vulcan-Co and Vulcan-LN_4–Co.

cannot be determined with the TGA analysis, as the exact ligand decomposition pathway is unknown. Still, the result does infer a minimal ligand loading of 2 wt% (full ligand decomposition assumed, partial decomposition suggests even higher mass loadings). A surface area loss is also observed after grafting, with a 50% decrease according to the nitrogen adsorption isotherm (Figure S1). The surface area loss might be associated with pore blockage and disruption of the N_2 adsorption monolayer by the anchored ligand. For Vulcan-LN_4–Co, there are additional mass losses, with the mass loss at 195 °C for the loss of coordinated solvent at the cobalt centre. There is also a higher mass loss at 300 °C, coming from the decomposition of the complex and possibly even the carbon surface, which is aided by the cobalt atoms. The anchored Co(bpb)OAc complex decomposition temperature agrees well with published values.[37] To determine the cobalt weight loading, we used elemental analysis, finding 2.1 wt% cobalt.

The high angle annular dark field image from the scanning transmission electron microscope (HAADF-STEM) of Vulcan-LN_4–Co does not show any cobalt nanoparticles (Figure 1b). This agrees with the elemental mapping from the energy dispersive X-ray spectroscopy (EDX) which shows no segregation of bulk cobalt species (Figure 1c, cobalt in red and carbon in green; the corresponding mapping of Co, N, O, and C of a different region is shown in Figure S2). The singular metal centers are visible under further magnification of the HAADF-STEM, which shows cobalt atoms as bright spots on the carbon surface (Figure 1d, a few sites circled in orange).

Electrode/active site interactions

The grafting was further confirmed by X-ray photoelectron spectroscopy (Figure 2a). Vulcan contains no nitrogen, but the N 1s XPS region of Vulcan-LN_4 shows a distinct peak combining the pyridine (399.7 eV) and amide (400.5 eV) functional groups, with a ratio close to 1:1 (corresponding to the ratio of functionalities in the ligand). A diazonium signal at 405 eV is absent, supporting the successful anchoring to the surface.[38] Upon forming the cobalt complex, the pyridine N 1s XPS peak shifts to higher binding energies (400.2 eV) due to the coordination of the cobalt centre. The amide is deprotonated, shifting the signal to lower binding energies, while the coordination with cobalt yields a positive shift.[39] This combination results in the signal at 399.0 eV. A similar peak shape is observed for Co(bpb)OAc, with two peaks at 398.2 (amide) and 399.6 eV (pyridine). The different N 1s binding energies for the anchored and free complex indicate different electronic structures.

We also see an electronic difference in the Co 2p XPS region (Figure 2b). The peaks for Co $2p_{3/2}$ and Co $2p_{1/2}$ of Vulcan-LN_4–Co are located at 781.3 eV and 797.0 eV, while Co(bpb)OAc has them at 781.4 eV and 797.3 eV. We see additional satellite peaks (786.0 eV and 802.9 eV) for Vulcan-LN_4–Co, indicating a Co(II) species. To ensure that these satellite peaks do not originate from cobalt precipitates introduced during the metallization reaction, we treated Vulcan XC-72R with Co-$(OAc)_2.4H_2O$ (Vulcan-Co). As the Vulcan-Co and Vulcan-LN_4–Co Co 2p XPS regions differ, we conclude that the satellite peaks are not from precipitates. Instead, the anchored species is in the Co(II) oxidation state, unlike the Co(III) of the free complex. As the Co(III) state has a coordinated acetate ligand, we also examined the O 1s signal of Co(bpb)OAc. Here, three peaks are fitted for the amide (533.1 eV), the acetate (531.8 eV) and the methanol/Co–O (530.6 eV) (Figure 2c).[40] At first glance, Vulcan-N_4–Co still has the acetate peak. However, oxidized carbon moieties from the Vulcan obscure the O 1s region, having a broad range of different signals (broad peaks at 533.8 and

531.9 eV).[41] Interestingly, Vulcan-N_4–Co lacks the Co–O feature associated with the methanol/Co–O. The exact reason for this is unknown. Even in a Co(II) oxidation state, a neutral axial ligand is expected when the cobalt centre is treated as a molecular system. We propose that the anchoring affects the need for a ligand as electron density could come from the carbon surface, allowing for the stabilization instead of a bound ligand. The lack of a Co–O feature also shows that the anchored complex does not readily oxidize when exposed to air, affirming the stability of the anchored complex.

More insight into the system was gained from the EPR studies. Vulcan has one broad and one sharp signal, both located at $g=2$, corresponding to organic radical species on the surface (Figure 2d). Both the Co(bpb) and Vulcan features are expected in the CW X-Band EPR spectrum of Vulcan-LN_4–Co. Indeed, overlaid onto the background signal of Vulcan we see a low-spin Co(II) signal, which fits to an isotropic tensor $g=$[2.62 2.31 2.04] similar to known Co(II)(bpb) complexes.[42] The low spin Co(II) feature is absent the CW X-Band EPR spectrum of Vulcan-Co. We conclude that the anchored complex is Co^{II}(bpb) rather than Co^{III}(bpb)OAc, confirming the electronic interaction.

Different electrochemical response

To study the electrode/active site interactions of the anchored complex, we analyzed the electrochemical response of Co-(bpb)OAc and Vulcan-LN_4–Co. We can distinguish between diffusion and adsorption based electron though recording cyclic voltammograms at different scan rates and plotting the current response against the scan rates (so-called trumpet plot).[43,44] For diffusion-controlled electron transfer (ET), the current is linear with the square root of the scan rate, while it is linear with the scan rate for adsorption based ET. The CV curves for Co-(bpb)OAc in a dichloromethane (DCM) electrolyte with 0.1 M $TBAPF_6$ show two reversible redox events (Figure 3a, and Figures S3 and S4). These are assigned to the oxidation/reduction of the cobalt centre [Co(III)↔Co(II), $E_{1/2}=-0.29$ V vs. Fc^+/Fc, a/a′] and [Co(II)↔Co(I), $E_{1/2}=-0.87$ V vs. Fc^+/Fc, b/b′], based on previous studies on Co(bpb) complexes.[45] As expected, the trumpet plot indicates a diffusion based electron transfer reaction (Figure S5). The small reductive peak located at −1.3 V vs. Fc^+/Fc is attributed to the reduction of residual oxygen in the electrolyte.

The anchored complex, Vulcan-LN_4–Co, exhibits no significant redox events in the DCM electrolyte (Figure 3b). A lack of redox events in conjugated molecular complexes was observed previously.[29,33] ET reactions for conjugated molecular catalysts are only observed if an ion transfer occurs. But the DCM $TBAPF_6$ electrolyte does not allow such reactions as no suitable ions are present (there are no protons and both TBA^+ and PF_6^- act more as counterions than coordinating species).[46] We deemed a lack of redox events as insufficient proof and thus also used an electrolyte which allows ionic transfer during ET reactions.

Thus, we again examined the redox behaviours in an aqueous phosphate buffer electrolyte (PBS, 0.1 M, pH = 7.0) with an excess of coordinating ions. Co(bpb)OAc is slightly soluble and exhibits two redox events, Co(III)↔Co(II) (0.75 V vs. RHE) and Co(II)↔Co(I) (0.4 V vs. RHE) (Figure 4a). However, the intensity and reversibility of these events have changed significantly from the DCM electrolyte. The first redox event at 0.75 V vs. RHE has a much lower intensity than the second event at 0.4 V vs. RHE, while both show higher reductive currents than oxidative currents. We speculate that the initial low solubility in the aqueous electrolyte of Co(bpb)OAc and variations in the solubility of the oxidation/reduction products in part explain the observed redox behaviours.

The CV curve for Vulcan-LN_4–Co in the 0.1 M PBS buffer shows three reversible redox events (Figure 4b and S6). Two of these are around the potential where the complex itself exhibits redox events, while the third occurs at higher potentials. The two events at $E_{1/2}=0.65$ V [Co(III)↔Co(II)] and $E_{1/2}=0.53$ V vs. RHE [Co(II)↔Co(I)] have peak separations <59 mV (± 30 mV at 20 mV s^{-1}), indicating that the species do not diffuse to and from the electrode. Furthermore, their trumpet plot confirms that these ET reactions are heterogeneous (Figure S7). The additional redox event at $E_{1/2}=1.04$ V vs. RHE, with a peak separation of >59 mV, can correspond to the oxidation of the ligand. Bpb is a non-innocent ligand that oxidizes at high oxidizing potentials.[45,47,48] While this event was not observed for Co(bpb)OAc, the ligand anchoring position is located at the carbon that bears the largest charge density for $bpb^{(ox)}$. Most likely, there is a large charge distribution towards the graphitic network. We expect thus a large potential shift, while the large peak separation is likely induced by the different local environments of the graphitic network. All these results support that

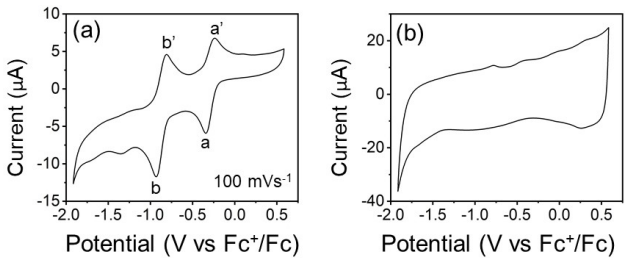

Figure 3. CV curves in argon saturated DCM 0.1 M $TBAPF_6$ electrolyte at a scan rate of 100 mV s^{-1} for (a) Co(bpb)OAc (1 mM) and (b) Vulcan-LN_4–Co.

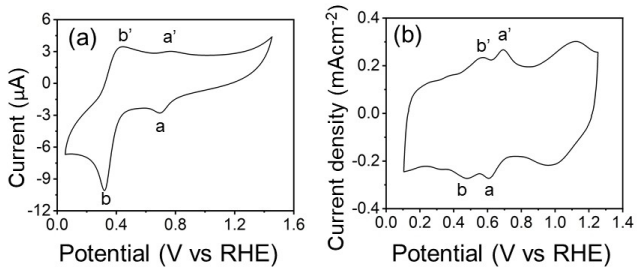

Figure 4. CV curves in argon saturated 0.1 M PBS aqueous electrolyte (pH = 7.0) at a scan rate of 100 mV s^{-1} for (a) Co(bpb)OAc (1 mM) and (b) Vulcan-LN_4–Co.

there is a strong electronic interaction between the electrode and organometallic complex.

ORR electrocatalysis

Vulcan-LN_4–Co shows unique performance in the oxygen reduction reaction (ORR). Theoretically, molecular oxygen can be reduced to water [$4e^-$ pathway, Eq. (1)] or to hydrogen peroxide [$2e^-$ pathway, Eq. (2)], with the possibility of further reduction of hydrogen peroxide to water [$2e^- + 2e^-$ pathway, Eq. (3)].

$$O_2 + 4H^+ + 4e^- \rightarrow 2H_2O \quad E_0 = 1.23\ \text{V vs. RHE} \tag{1}$$

$$O_2 + 2H^+ + 2e^- \rightarrow H_2O_2 \quad E_0 = 0.695\ \text{V vs. RHE} \tag{2}$$

$$H_2O_2 + 2H^+ + 2e^- \rightarrow 2H_2O \quad E_0 = 1.76\ \text{V vs. RHE} \tag{3}$$

The ORR activity of both Co(bpb)OAc and Vulcan-LN_4–Co were measured in an aqueous 0.1 M phosphate buffer (pH = 7.0) saturated with oxygen (Figure 5a). Both exhibit reductive waves at an onset potential of 0.68 V and 0.78 V vs. RHE for Co(bpb)OAc and Vulcan-LN_4–Co, respectively (derived from where the extrapolated linear part of the redox current intersects the x-axis). These are absent in the earlier experiments with argon saturated 0.1 M PBS buffer and are thus attributed to ORR. Note that the currents are normalized for clarity and the original current of Co(bpb)OAc is significantly lower than Vulcan-LN_4–Co (see inset of Figure 5a). The higher current for Vulcan-LN_4–Co is a combination of a high surface concentration of the bound organometallic complex and the enhanced electrode/active site interaction. The latter is also responsible for the lower ORR onset potential for Vulcan-LN_4–Co compared to Co(bpb)OAc, as observed elsewhere.[49,50]

To evaluate the H_2O_2 selectivity of ORR, we used a rotating ring disk electrode (RRDE) setup.[51,52] The cyclic voltammetry was obtained in both argon and oxygen saturated electrolyte to ensure that the observed currents are from ORR (Figure S8–11). Vulcan-LN_4–Co has an ORR onset potential of 0.72 V vs. RHE at a current density of 0.1 mA cm^{-2} (Figure S12). Note that the abovementioned 0.78 V onset potential is derived through extrapolation of the redox current. The anchored complex is the active site for ORR, as Vulcan, Vulcan-LN_4 and Vulcan-Co all showed lower onset potentials (Figure S12). The linear sweep voltammetry of Vulcan shows an ORR onset potential of 0.47 V vs. RHE. Interestingly, Vulcan-LN_4 performed worse than pure Vulcan (onset potential of 0.41 V vs. RHE), which is attributable to the catalytic inert nature of the LN_4 complex which blocks the active sites of carbon (see the surface area loss in Figure S2). Vulcan-Co has the same onset potential as Vulcan, proving the ORR activity of Vulcan-LN_4–Co does not originate from other adsorbed cobalt species on the surface.

H_2O_2 oxidation on the Pt ring (set at 1.2 V vs. RHE, rotation of 1600 rpm) was observed for all samples. Carbon materials preferentially catalyse the 2-electron ORR towards H_2O_2 (Figure S12). The conversion of the platinum current response shows that Vulcan-LN_4–Co achieves a maximum H_2O_2 selectivity of 80% in the 0.45–0.72 V vs. RHE range (Figure 5b). Note that this onset potential is higher than the theoretical Nernst potential which is calculated at the standard conditions. But hydrogen peroxide is absent at the start of the electrochemical experiments. This yields an additional drive in the form of a higher reduction potential for the O_2 to H_2O_2 ORR reaction.[53]

At higher applied overpotentials, the H_2O_2 selectivity decreases as the $2e^- + 2e^-$ pathway becomes more viable. The active sites for the $2e^- + 2e^-$ pathway are not likely to be located at the carbon support, as both Vulcan and Vulcan-LN_4 have increased H_2O_2 selectivity's when going to more cathodic potentials. The H_2O_2 selectivity of Vulcan-Co (which has 1.7 wt% cobalt based on elemental analysis) is low, confirming that cobalt alone preferentially catalyse ORR towards water. Quantifying the H_2O_2 selectivity of the Co(bpb)OAc complex in solution is difficult, as it acts as a redox mediator and is oxidized at the platinum ring, yielding a parasitic current besides the H_2O_2 oxidation current.

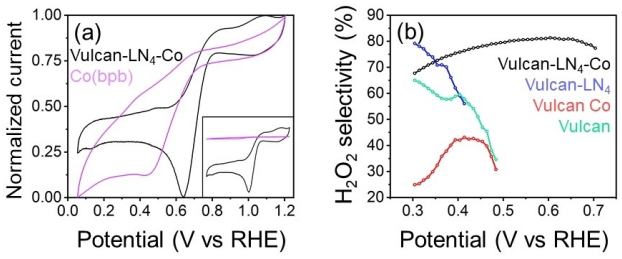

Figure 5. (a) Normalized voltammograms of the Co(bpb)OAc and Vulcan-LN_4–Co in an oxygen saturated 0.1 M PBS electrolyte, inset showing the non-normalized data, at a scan rate of 10 mV s^{-1}, and (b) hydrogen peroxide selectivity calculated from the Disk and Ring currents.

Theoretical study of the ORR activity

Further insight into the ORR activity and selectivity of the Vulcan-LN_4–Co catalyst was gained through density functional theory (DFT) studies at the BP86/def2-TZVP/disp3/m4 level of theory (see computational details in the Supporting Information). We note that the conjugated linkage of the molecular complex and surface results in a more metallic electrochemical mechanism. Still, we assume that ORR occurs on the cobalt centre and electrons are still transferred via the cobalt atom to the substrate. As such, we use a simplified model system for the calculations based on the crystal structure derived from single crystal X-ray diffraction (Figure S12). The [Co^{II}(bpb)]·H_2O complex (abbreviated as Co^{II}(bpb), Figure 4b) has a Co(II) starting oxidation state as the ORR onset potential coincides with the Co(III)↔Co(II) reduction. Since all experiments were performed in aqueous solutions, we assume the axial coordination of water and took this into account in our model system. Furthermore, the end-on coordination of the $*O_2$ and *OOH reaction intermediates to cobalt was observed to be most stable (Table S5). End-on coordination is typically observed for isolated active centres, i.e., cobalt, of discrete metal complexes.[54–56]

Our proposed mechanism for ORR on Co^{II}(bpb) proceeds via similar intermediates in both the $2e^-$ and $4e^-$ pathway (Scheme 2). In both pathways oxygen is activated by absorbance (coordination) onto cobalt (*) in an exergonic manner (−0.20 eV, Table S8). This affords the Co(III)-superoxide intermediate ($*O_2$, step A in Scheme 2). Subsequent proton-coupled electron transfer (PCET) on the farther oxygen atom results in the formation of the *OOH intermediate [Eq. (4) and step B in Scheme 2]. At this point the catalytic cycle diverges between the $4e^-$ and $2e^-$ pathway. The $4e^-$ pathway continues with PCET on the protonated oxygen atom, affording one equivalent of water and the *O intermediate [Eq. (5) and step D in Scheme 2]. Notably, the cobalt complex changes from low spin to intermediate spin and reorganizes from a 6-coordinated octahedral to a 5-coordinated distorted trigonal bipyramidal configuration. The 6-coordinated octahedron re-forms after the next PCET, with the formation of the *OH intermediate [Eq. (6) and step E in Scheme 2]. The final PCET step yields another equivalent of water and the low spin Co^{II}(bpb) starting complex [Eq. (7) and step F in Scheme 2]. In contrast, PCET in the $2e^-$ pathway occurs on the oxygen atom which is not yet hydrogenated and coordinated to the active site [Eq. (8) and step C in Scheme 2]. Consequently, hydrogen peroxide is released and the Co^{II}(bpb) starting complex is regenerated.

$$^*O_2 + (H^+ + e^-) \rightarrow {}^*OOH \quad (4)$$

$$^*OOH + (H^+ + e^-) \rightarrow H_2O + {}^*O \quad (5)$$

$$^*O + (H^+ + e^-) \rightarrow {}^*OH \quad (6)$$

$$^*OH + (H^+ + e^-) \rightarrow H_2O + {}^* \quad (7)$$

$$^*OOH + (H^+ + e^-) \rightarrow H_2O_2 + {}^* \quad (8)$$

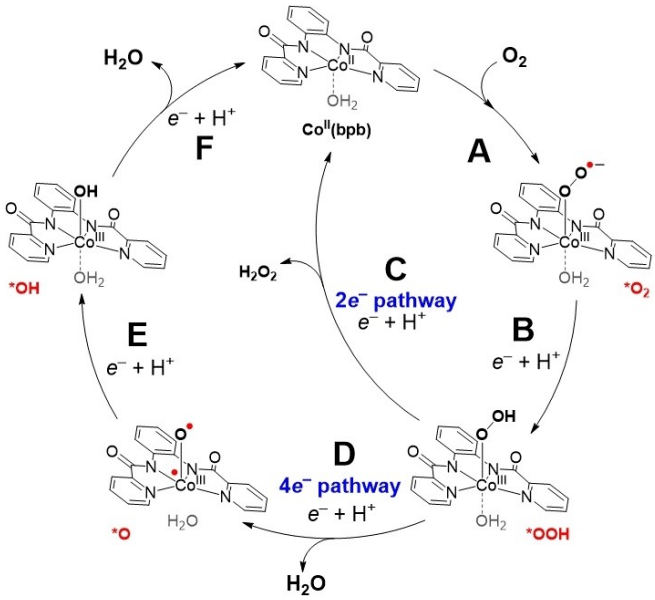

Scheme 2. The proposed mechanism for ORR on Co^{II}(bpb) via the $2e^-$ and $4e^-$ pathway electron pathways.

Concerning this $2e^-$ pathway, we assume that a catalyst provides high activity by minimizing the kinetic barriers for Equation (4) and Equation (8). Furthermore, high selectivity must be achieved by maximizing the barrier for *OOH reduction and subsequent dissociation to *O [Eq. (5)] and *OH [Eq. (6)].[57] The binding free energy for *OOH ($\triangle G_{*OOH}$) is an effective descriptor of catalyst activity for the two-electron ORR.[57] More specifically, for effective hydrogen peroxide selective ORR catalysis, the *OOH binding should follow the Sabatier principle. Based on our calculations, we found a *OOH binding free energy of 4.34 eV for the Co^{II}(bpb) catalyst (Table S9). This value is close to the theoretical ideal binding free energy for *OOH, which is $\triangle G_{*OOH} = \sim 4.2 \pm 0.2$ eV under zero potential versus RHE.[57–60] This near-ideal binding free energy enables the high selectivity of the Co^{II}(bpb) catalyst towards hydrogen peroxide.

With respect to the catalyst selectivity, the O–O bond scission is closely related to the binding strengths of the intermediates of the $4e^-$ pathway: *OH and *O.[57] Namely, a weaker interaction between the cobalt site and these intermediates results in a higher selectivity to H_2O_2. Given that the binding free energy of *OOH scales linearly with that of *OH (3.2 ± 0.2 eV),[61,62] the ideal binding free energy of *OH is $\triangle G_{*OH} = \sim 1.0 \pm 0.2$ eV under zero potential versus RHE. When the binding free energy exceeds ~1.0 eV, the *OH intermediate, and consequently the *O intermediate are less likely to form due to the low oxygen affinity of the cobalt site.[57] Our calculations gave a binding free energy of $\triangle G_{*OH} = 1.12$ eV for the Co^{II}(bpb) catalyst. Thus, besides the close to ideal $\triangle G_{*OOH}$, there is a low affinity for the *OH intermediate of the $4e^-$ pathway, further supporting a $2e^-$ pathway.

The above-discussed principles are visualized in Figure 6a, showing the theoretical oxygen reduction volcano plot as adapted from ref.[51] On the lower horizontal axis, the limiting potential is plotted as a function of $\triangle G_{*OH}$, while the upper horizontal axis plots the $\triangle G_{*OOH}$. The two horizontal axes are connected through their linear scaling relations as mentioned above. In this figure, the horizontal dotted lines present the equilibrium potential for the $2e^-$ pathway, $U^0_{O_2/H_2O_2}$, and the $4e^-$ pathway, $U^0_{O_2/H_2O}$, respectively. The blue and red lines represent the correlation between the $\triangle G_{*OH}$ and $\triangle G_{*OOH}$, and the limiting potential for the $2e^-$ and $4e^-$ reduction of oxygen, respectively.

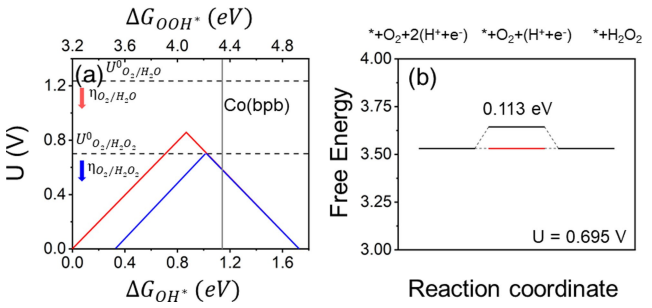

Figure 6. (a) A volcano plot for the $2e^-$ (blue) and $4e^-$ (red) pathway adapted from ref. [51], with their corresponding theoretic potentials (dashed lines). The gray line indicates our calculated binding energies for *OOH and *OH of Co(bpb). (b) Free energy diagram for the approximation of the energy barrier of Co(bpb) for the $2e^-$ pathway at 0.695 V.

Based on the calculated binding free energies, the Co^{II}(bpb) catalyst (in grey) lies on the right side of the peak of the $2e^-$ volcano. This side indicates the binding energies where breaking the O–O bond and forming the HO* and O* intermediates is more difficult. Consequently, a higher selectivity towards hydrogen peroxide is achieved, at the expense of activity.[57]

Lastly, we calculated the free energy diagram (FED) for the $2e^-$ pathway using Nørskov's method[63] (see computational details in the Supporting Information). At the equilibrium potential ($U = 0.695$ V) an ideal catalyst would display high current densities at negligible overpotentials, i.e., the FED is flat at the equilibrium potential as shown in Figure 6b (in red). For the Co^{II}(bpb) catalyst, the formation of the *OOH intermediate is only slightly endergonic (~0.1 eV, Figure 6b, in black). Since *OOH formation is the potential determining step (PDS), this relatively low formation energy resembles the efficient ORR activity for hydrogen peroxide formation.[54,57,64]

Altogether, the hydrogen peroxide selectivity of the Co^{II}-(bpb) catalyst can be explained by the relatively low overpotential required for the formation of the *OOH intermediate, in addition to its close to ideal calculated binding free energy ($\triangle G_{*OOH}$). The selectivity follows from the binding free energy of the *OH intermediate ($\triangle G_{*OH}$), which indicates a relatively weak interaction. Consequently, the $2e^-$ pathway is favoured over the $4e^-$ pathway.

Conclusions

We developed a synthetic approach of constructing conjugated C–C bonding between a carbon surface and an organometallic cobalt catalyst. The induced strong interaction between the electrode and the molecular catalysts enables rapid electron transfer and optimized electronic structure of the cobalt active centre. The anchored catalyst is highly selective (80%) in the oxygen reduction reaction (ORR) towards hydrogen peroxide in neutral media at almost no overpotential (0.72 V vs. RHE at 0.1 mA cm^{-2}). Density functional theory (DFT) calculations affirm this electrocatalytic performance by showing a *OOH binding free energy close to the optimum (4.34 eV vs. 4.20 eV), a low affinity for the *OH intermediate and a slightly endergonic *OOH formation energy at the theoretical onset potential. Overall, this is an effective approach of immobilizing molecular catalysts on carbon without inducing negative effect, opening new avenues for the practical applications of molecular catalysts in electrochemical devices.

Experimental Section

Materials characterizations

Infrared spectra were measured on a Thermo Scientific Nicolet iS50 FT-IR equipped with a Specac Quest with a diamond puck ATR. The ATR was purged with dry N_2 before analysis. Thermogravimetric analysis was performed on a Netzsch STA 449 F3 Jupiter, using an argon atmosphere, 40 mL min^{-1} flowrate and a heating rate of 5 K min^{-1}. Nitrogen adsorption isotherms were collected on a Belsorp-maxII. Samples for nitrogen adsorption were prepared in a Belprep-vacIII, at 200 °C under vacuum for 6 h. Nuclear Magnetic Resonance spectra were recorded on a Bruker AV300. Electrochemical experiments were performed with a Gamry reference 600 potentiostat. X-ray intensities were measured on a Bruker D8 Quest Eco diffractometer equipped with a Triumph monochromator ($\lambda = 0.71073$ Å) and a CMOS Photon 100 detector at a temperature of 150 K. Scanning electron microscopy was performed on a JEOL JSM-6010LA. For X-ray photoelectron spectroscopy (XPS) a Kratos AXIS equipped with monochromatic Al Kα X-ray source was used and the base pressure in the analytical chamber was 10^{-9} mbar. ICP analysis was performed by Kolbe Labs GmbH.

Preparation of bpb ligand [N,N′-(1,2-phenylene)dipicolinamide]

1,2-phenylenediamine (325 mg, 3 mmol) and picolinic acid (1100 mg, 9 mmol) were dissolved in 5 mL pyridine. To this solution, triphenylphosphite (2.35 mL, 9 mmol) was added and refluxed overnight. After cooling down to rt, the solution was poured in 200 mL DI H_2O. The white/brown suspension was vacuum filtered, washed with methanol and water, till the filtrate turned colorless. The off-white solid was recrystallized from MeOH, yielding white crystals, dried at 40 °C in vacuum overnight. ^{1}H-NMR (300 MHz. DMSO-d_6) δ 10.76 (s, 2H), 8.58 (d, $J = 4.3$ Hz, 2H), 8.21 (d, $J = 7.8$ Hz, 2H), 8.10 (dt, $J = 7.6$, 1.7 Hz, 2H), 7.82 (dd, $J = 6.0$, 3.5 Hz, 2H), 7.71 (ddd, $J = 7.5$, 4.8, 1.2 Hz, 2H), 7.34 (dd, $J = 6.0$, 3.4 Hz, 2H)

Preparation of Co(bpb)OAc complex

Dissolved bpb ligand [N,N′-(1,2-phenylene)dipicolinamide] (100 mg, 0.32 mmol) in 4 mL MeOH, while heating to 60 °C and added trimethylamine (45 μL, 0.32 mmol). Dissolved $Co(OAc)_2.4H_2O$ (80 mg, 0.32 mmol) in 1 mL DI H_2O and added the $Co(OAc)_2$ to the bpb solution, instantaneously turning brown. The solution was cooled to 4 °C for 5 days and the brown/green solid crystals collected via filtration, washing with DI H_2O and cold MeOH, dried at 40 °C in vacuum overnight. ^{1}H-NMR (300 MHz. DMSO-d_6) δ 10.15 (d, $J = 5.2$ Hz, 2H), 8.94 (dd, $J = 6.0$, 3.5 Hz, 2H), 8.34 (dt, $J = 7.6$, 1.2 Hz, 2H), 8.13 (dd, $J = 7.7$, 1.3 Hz, 2H), 7.94 (dt, $J = 5.6$, 1.6 Hz, 2H), 7.07 (dd, $J = 6.0$, 3.5 Hz, 2H), 4.13 (q, $J = 5.1$ Hz, 1H), 3.21 (d, $J = 5.4$ Hz, 3H), 1.10 (s, 3H).

Single crystals were grown via a heated super saturated MeOH solution, slowly cooling down and crystallization at −18 °C for two weeks.

Preparation of bpb-NO_2 ligand [N,N′-(4-nitro-1,2-phenylene)dipicolinamide]

4-Nitro-1,2-phenylenediamine (612 mg, 4 mmol) and picolinic acid (2600 mg, 20 mmol) were dissolved in 10 mL pyridine. To this solution, triphenylphosphite (9.8 mL, 37.5 mmol) was added and refluxed overnight. After cooling down to rt, the solution was poured in 200 mL MeOH. The brown suspension was vacuum filtered, washed with methanol and water, till the filtrate turned from yellow till colorless, yielding a pale-yellow solid, dried at 40 °C in vacuum overnight. ^{1}H-NMR (300 MHz. DMSO-d_6) δ 11.09 (s, 2H), 8.77 (d, $J = 4.4$ Hz, 1H), 8.70–8.67 (m, 2H), 8.27–8.17 (m, 4H), 8.13 (tt, $J = 7.7$, 1.6 Hz, 2H), 7.75 (ddd, $J = 10.8$, 6.0, 1.2 Hz, 2H)

Preparation of bpb-NH_2 ligand [N,N′-(4-amino-1,2-phenylene)dipicolinamide]

In a nitrogen atmosphere, palladium on carbon (5 wt%, 50% wet, 40 mg) was suspended in 40 mL methanol and bpb-NO_2 ligand [N,N′-(4-nitro-1,2-phenylene)dipicolinamide] (400 mg) was added to the Pd/C suspension. Hydrogen was introduced in the reaction mixture and the reaction was stirred with a hydrogen atmosphere overnight. The black suspension was filtered, and the methanol was evaporated from the yellow filtrate, yielding a dark yellow solid, dried at 40 °C in vacuum overnight. ^{1}H-NMR (300 MHz. DMSO-d_6) δ 10.47 (s, 1H), 10.39 (s, 1H), 8.70 (qd, J = 4.7, 1.0 Hz, 1H), 8.57 (qd, J = 4.7, 1.0 Hz, 1H), 8.20–8.14 (m, 2H), 8.07 (tt, J = 7.5, 1.6 Hz, 2H), 7.24 (d, J = 3.9 Hz, 1H), 7.22 (d, J = 2.1 Hz, 1H), 6.50 (dd, J = 8.5, 2.5 Hz, 1H), 5.26 (bs, 2H)

Anchoring the organic linker to Vulcan

bpb-NH_2 ligand [N,N′-(4-amino-1,2-phenylene)dipicolinamide] (67 mg, 0.2 mmol) was added to 10 mL DI water and 2 mL HCl (37%). Sodium nitrite (28 mg, 0.4 mmol) was added, turning the pale-yellow solution dark yellow, with minor gas evolution. Vulcan XC-72R (200 mg) was added and the suspension was stirred overnight. The suspension was filtered and washed with 100 mL DI water, 100 mL Ethanol, 100 mL DMF, 100 mL acetone, 50 mL DMSO and 100 mL acetone, with the filtrate changing from red to colorless. The solid was dried at 40 °C in vacuum for 18 hours.

Forming the Co(bpb)OAc complex on the functionalized Vulcan

Suspended the functionalized Vulcan (50 mg) in 2 mL MeOH, added trimethylamine (5 μL) and heated to 60 °C. $Co(OAc)_2.4H_2O$ (5 mg) was dissolved in 1 mL DI water and the solution was added to the carbon suspension. This was heated at 60 °C overnight, where after it was filtered and washed with copious amounts of DI water, till the filtrate turned from brown to colorless. The material was dried at 120 °C for 18 hours.

X band EPR

EPR measurements were performed in quartz tubes in an atmosphere of purified nitrogen at 10 K. Co(bpb)OAc was measured in a 9:1 MeOH/EtOH glass. The solid Vulcan samples were diluted with KBr. EPR spectra were recorded on a Bruker EMX-plus CW X-band spectrometer equipped with a Bruker ER 4112HV-CF100 helium cryostat. The spectra were obtained on freshly prepared solutions of 1–10 mM compound and simulated using EasySpin[65] via the cwEPR GUI.[66]

Catalyst ink for electrochemical experiments

Catalyst inks were prepared by suspending the catalysts (1 mg) in an ethanol (1 mL) with 10 μL Nafion® (D-521 dispersion 5 wt.% in water/isopropanol) and sonicated for 18 hours.

Electrochemical experiments for the oxygen reduction reaction

The oxygen reduction reaction was measured in a standard three-electrode system. A rotating ring disk electrode (RRDE, Pine research 0.2475 cm^2 glassy carbon disk, 0.1866 cm^2 platinum ring) was first polished and the catalyst was added by drop casting 3 times with 10 μL of catalyst ink and drying in air between drops. A saturated calomel electrode (SCE) and a graphite rod were used as the reference and counter electrodes, respectively. The 0.1 M phosphate buffer electrolyte was saturated with oxygen and maintained at 25 °C. Blank experiments were performed in a 0.1 M phosphate buffer electrolyte purged with argon and maintained at 25 °C. Cyclic voltammetry (CV) curves were recorded at 10 mV s^{-1}. Linear sweep voltammetry (LSV) curves were recorded at 10 mV s^{-1}. For RRDE experiments, the electrode was rotated at 1600 rpm and the platinum ring was held at a constant potential of 1.2 V vs. RHE. The disk was swept with a 10 mV s^{-1} scan rate. The hydrogen peroxide selectivity at a given potential was calculated from the disk and ring current (I_D and I_R, respectively) through Equation (9):

$$H_2O_2[\%] = 200 \times \frac{I_R/N}{I_D + I_R/N} \quad (9)$$

were N is the current collection efficiency of the ring. This current collection efficiency was determined by the reversible oxidation/reduction of $[Fe(CN)_6]^{4-}/[Fe(CN)_6]^{3-}$ redox pair under different rotation speeds.

Electrochemical experiments for the investigation of the redox events of Co(bpb)OAc

Investigations of the redox events of Co(bpb)OAc were performed in a H-cell, using a glassy carbon electrode (0.07 cm^{-2}), platinum wire counter electrode, Nafion® membrane and SCE reference electrode. The dichloromethane electrolyte contained 0.1 M $TBAPF_6$ and the working electrode chamber contained an additional 1 mM of Co(bpb)OAc, and was saturated with argon before use. To accurately determine the applied potential, the system was calibrated against the ferrocene/ferrocenium cation redox couple. For the study in aqueous media, a 0.1 M PBS buffer with 1 mM Co(bpb)OAc saturated with argon was used in the H-cell.

Electrochemical experiments for the investigation of the redox events of Vulcan-LN_4–Co

Investigation of the redox events of Vulcan-LN_4–Co in organic electrolyte were performed in a H-cell assembly, using a glassy carbon electrode (0.07 cm^{-2}), platinum wire counter electrode, Nafion® membrane and SCE reference electrode. The glassy carbon electrode was drop casted 10 times with 1 μL catalyst ink and air dried in between. The dichloromethane electrolyte contained 0.1 M $TBAPF_6$, and the working electrode chamber was saturated with argon before use. To accurately determine the applied potential, the system was calibrated against the ferrocene/ferrocenium cation redox couple. The investigation of the redox events in aqueous media was performed in a standard three-electrode system. A rotating ring disk electrode (RRDE, Pine research 0.2475 cm^2 glassy carbon disk, 0.1866 cm^2 platinum ring) was first polished and the catalyst was added by drop casting 3 times with 10 μL of catalyst ink and drying in air between drops. A saturated calomel electrode (SCE) and a graphite rod were used as the reference and counter electrodes, respectively. The 0.1 M phosphate buffer electrolyte was saturated with argon before use.

DFT calculations

DFT geometry optimizations were performed on full atomic models (no simplifications) using TURBOMOLE 7.5.1[67] coupled to the PQS Baker optimizer[68] via the BOpt package.[69] All calculations were performed in the gas phase at the BP86[70]/def2-TZVP[71,72] level of theory (unless stated otherwise) with strict convergence criteria

(scfconv = 7) on a m4 grid. In addition, Grimme's version 3 (disp3, "zero damping") dispersion corrections were applied.[73] All minima (no imaginary frequencies) were characterized by numerically calculating the Hessian matrix. The final energy evaluation was performed with single point calculations at the BP86/def2-QZVPPD level of theory (unless stated otherwise) with strict convergence criteria (scfconv = 9) on a m5 grid, using Grimme's version 3 (disp3, "zero damping") dispersion corrections. The energy output was reported in Hartree and was converted to eV by multiplication with 27.2114 and to kcal mol^{-1} by multiplication with 627.5.

When applicable, corrected broken symmetry energies (ε_{BS}) of the open-shell singlets ($S = 0$) were estimated from the energy (ε_S) of the optimized single-determinant broken symmetry solution and the energy (ε_{S+1}) from a separate unrestricted triplet state single-point calculation at the same level, using the approximate correction Equation (10).

$$\varepsilon \approx \frac{S_{S+1}^2 \times \varepsilon_S - S_S^2 \times \varepsilon_{S+1}}{S_{S+1}^2 - S_S^2} \quad (10)$$

Supporting Information

The authors have cited additional references within the supporting information.[74–79]

Acknowledgements

We thank the Netherlands Organization for Scientific Research (NWO) for financial support through the NWO-GDST Advanced Materials program (project No. 729.001.022) and NWO-Vidi grant (VI.Vidi.192.045). This work is part of the Research Priority Area Sustainable Chemistry of the UvA, http://suschem.uva.nl.

Conflict of Interests

The authors declare no conflict of interest.

Data Availability Statement

The data that support the findings of this study are available from the corresponding author upon reasonable request.

Keywords: organometallics · strong interaction · immobilization · electrochemistry · neutral media

[1] H. S. Taylor, *Proc. R. Soc. Lond. Ser. Contain. Pap. Math. Phys. Character* **1925**, *108*, 105–111.
[2] J. K. Nørskov, T. Bligaard, B. Hvolbæk, F. Abild-Pedersen, I. Chorkendorff, C. H. Christensen, *Chem. Soc. Rev.* **2008**, *37*, 2163–2171.
[3] G. A. Somorjai, K. R. McCrea, J. Zhu, *Top. Catal.* **2002**, *18*, 157–166.
[4] C. Vogt, B. M. Weckhuysen, *Nat. Chem. Rev.* **2022**, *6*, 89–111.
[5] W. A. Herrmann, B. Cornils, *Angew. Chem. Int. Ed.* **1997**, *36*, 1048–1067.
[6] S. Z. Tasker, E. A. Standley, T. F. Jamison, *Nature* **2014**, *509*, 299–309.
[7] P. Serna, B. C. Gates, *Acc. Chem. Res.* **2014**, *47*, 2612–2620.
[8] J. Artz, *ChemCatChem* **2018**, *10*, 1753–1771.
[9] I. M. Denekamp, C. Deacon-Price, Z. Zhang, G. Rothenberg, *Catal. Sci. Technol.* **2020**, *10*, 6694–6700.
[10] R. Raja, J. M. Thomas, M. D. Jones, B. F. G. Johnson, D. E. W. Vaughan, *J. Am. Chem. Soc.* **2003**, *125*, 14982–14983.
[11] E. Le Roux, Y. Liang, R. Anwander, *ChemCatChem* **2018**, *10*, 1905–1911.
[12] J. Lu, P. Serna, C. Aydin, N. D. Browning, B. C. Gates, *J. Am. Chem. Soc.* **2011**, *133*, 16186–16195.
[13] K. Torbensen, D. Joulié, S. Ren, M. Wang, D. Salvatore, C. P. Berlinguette, M. Robert, *ACS Energy Lett.* **2020**, *5*, 1512–1518.
[14] C. C. L. McCrory, A. Devadoss, X. Ottenwaelder, R. D. Lowe, T. D. P. Stack, C. E. D. Chidsey, *J. Am. Chem. Soc.* **2011**, *133*, 3696–3699.
[15] R. M. Bullock, A. K. Das, A. M. Appel, *Chem. Eur. J.* **2017**, *23*, 7626–7641.
[16] S. A. Yao, R. E. Ruther, L. Zhang, R. A. Franking, R. J. Hamers, J. F. Berry, *J. Am. Chem. Soc.* **2012**, *134*, 15632–15635.
[17] W. Zhang, A. U. Shaikh, E. Y. Tsui, T. M. Swager, *Chem. Mater.* **2009**, *21*, 3234–3241.
[18] M. Wang, K. Torbensen, D. Salvatore, S. Ren, D. Joulié, F. Dumoulin, D. Mendoza, B. Lassalle-Kaiser, U. Işci, C. P. Berlinguette, M. Robert, *Nat. Commun.* **2019**, *10*, 3602.
[19] W. Zhang, L. Wang, L.-H. Zhang, D. Chen, Y. Zhang, D. Yang, N. Yan, F. Yu, *ChemSusChem* **2022**, *15*, e202200195.
[20] P. Hutchison, R. E. Warburton, Y. Surendranath, S. Hammes-Schiffer, *J. Phys. Chem. Lett.* **2022**, *13*, 11216–11222.
[21] Y. Zhou, Y.-F. Xing, J. Wen, H.-B. Ma, F.-B. Wang, X.-H. Xia, *Sci. Bull.* **2019**, *64*, 1158–1166.
[22] S. Cho, J. M. Lim, J.-M. You, S. Jeon, D. Kim, *Isr. J. Chem.* **2016**, *56*, 169–174.
[23] C. J. Kaminsky, S. Weng, J. Wright, Y. Surendranath, *Nat. Catal.* **2022**, *5*, 430–442.
[24] W. Zhang, E. J. Meeus, L. Wang, L.-H. Zhang, S. Yang, B. de Bruin, J. N. H. Reek, F. Yu, *ChemSusChem* **2022**, *15*, e202102379.
[25] X. Li, H. Lei, J. Liu, X. Zhao, S. Ding, Z. Zhang, X. Tao, W. Zhang, W. Wang, X. Zheng, R. Cao, *Angew. Chem. Int. Ed.* **2018**, *57*, 15070–15075.
[26] K. Chen, K. Liu, P. An, H. Li, Y. Lin, J. Hu, C. Jia, J. Fu, H. Li, H. Liu, Z. Lin, W. Li, J. Li, Y.-R. Lu, T.-S. Chan, N. Zhang, M. Liu, *Nat. Commun.* **2020**, *11*, 4173.
[27] A. Morozan, S. Campidelli, A. Filoramo, B. Jousselme, S. Palacin, *Carbon* **2011**, *49*, 4839–4847.
[28] K. L. Materna, R. H. Crabtree, G. W. Brudvig, *Chem. Soc. Rev.* **2017**, *46*, 6099–6110.
[29] M. N. Jackson, Y. Surendranath, *Acc. Chem. Res.* **2019**, *52*, 3432–3441.
[30] T. Fukushima, W. Drisdell, J. Yano, Y. Surendranath, *J. Am. Chem. Soc.* **2015**, *137*, 10926–10929.
[31] N. D. Ricke, A. T. Murray, J. J. Shepherd, M. G. Welborn, T. Fukushima, T. Van Voorhis, Y. Surendranath, *ACS Catal.* **2017**, *7*, 7680–7687.
[32] M. N. Jackson, M. L. Pegis, Y. Surendranath, *ACS Cent. Sci.* **2019**, *5*, 831–841.
[33] S. Oh, J. R. Gallagher, J. T. Miller, Y. Surendranath, *J. Am. Chem. Soc.* **2016**, *138*, 1820–1823.
[34] D. Eisenberg, W. Stroek, N. J. Geels, C. S. Sandu, A. Heller, N. Yan, G. Rothenberg, *Chem. Eur. J.* **2016**, *22*, 501–505.
[35] A. T. Masheter, L. Xiao, G. G. Wildgoose, A. Crossley, J. H. Jones, R. G. Compton, *J. Mater. Chem.* **2007**, *17*, 3515–3524.
[36] A. T. Masheter, G. G. Wildgoose, A. Crossley, J. H. Jones, R. G. Compton, *J. Mater. Chem.* **2007**, *17*, 3008–3014.
[37] R. L. Chapman, R. S. Vagg, *Inorg. Chim. Acta* **1979**, *33*, 227–234.
[38] P. Finn, W. L. Jolly, *Inorg. Chem.* **1972**, *11*, 1434–1435.
[39] C. Cauletti, L. Sestili, R. Zanoni, *Inorg. Chim. Acta* **1988**, *147*, 237–242.
[40] O. Pérez, O. F. Odio, E. Reguera, *New J. Chem.* **2022**, *46*, 11255–11265.
[41] J. Biemolt, G. Rothenberg, N. Yan, *Inorg. Chem. Front.* **2020**, *7*, 177–185.
[42] H. Baydoun, S. Mazumder, H. B. Schlegel, C. N. Verani, *Chem. Eur. J.* **2017**, *23*, 9266–9271.
[43] D. H. Evans, K. M. O'Connell, R. A. Petersen, M. J. Kelly, *J. Chem. Educ.* **1983**, *60*, 290.
[44] N. Elgrishi, K. J. Rountree, B. D. McCarthy, E. S. Rountree, T. T. Eisenhart, J. L. Dempsey, *J. Chem. Educ.* **2018**, *95*, 197–206.
[45] M. Ray, R. N. Mukherjee, *Polyhedron* **1992**, *11*, 2929–2937.
[46] W. Beck, K. Suenkel, *Chem. Rev.* **1988**, *88*, 1405–1421.
[47] S. Meghdadi, K. Mereiter, M. Amirnasr, F. Karimi, A. Amiri, *Polyhedron* **2014**, *68*, 60–69.
[48] S. K. Dutta, U. Beckmann, E. Bill, T. Weyhermüller, K. Wieghardt, *Inorg. Chem.* **2000**, *39*, 3355–3364.
[49] C. J. Kaminsky, J. Wright, Y. Surendranath, *ACS Catal.* **2019**, *9*, 3667–3671.
[50] J. Meng, H. Lei, X. Li, J. Qi, W. Zhang, R. Cao, *ACS Catal.* **2019**, *9*, 4551–4560.
[51] L. Müller, L. Nekrassow, *Electrochim. Acta* **1964**, *9*, 1015–1023.

[52] K. Jiang, S. Back, A. J. Akey, C. Xia, Y. Hu, W. Liang, D. Schaak, E. Stavitski, J. K. Nørskov, S. Siahrostami, H. Wang, *Nat. Commun.* **2019**, *10*, 3997.
[53] H. W. Kim, M. B. Ross, N. Kornienko, L. Zhang, J. Guo, P. Yang, B. D. McCloskey, *Nat. Catal.* **2018**, *1*, 282–290.
[54] K. Dong, J. Liang, Y. Ren, Y. Wang, Z. Xu, L. Yue, T. Li, Q. Liu, Y. Luo, Y. Liu, S. Gao, M. S. Hamdy, Q. Li, D. Ma, X. Sun, *J. Mater. Chem. A* **2021**, *9*, 26019–26027.
[55] M. L. Pegis, C. F. Wise, D. J. Martin, J. M. Mayer, *Chem. Rev.* **2018**, *118*, 2340–2391.
[56] X.-P. Zhang, A. Chandra, Y.-M. Lee, R. Cao, K. Ray, W. Nam, *Chem. Soc. Rev.* **2021**, *50*, 4804–4811.
[57] S. Siahrostami, A. Verdaguer-Casadevall, M. Karamad, D. Deiana, P. Malacrida, B. Wickman, M. Escudero-Escribano, E. A. Paoli, R. Frydendal, T. W. Hansen, I. Chorkendorff, I. E. L. Stephens, J. Rossmeisl, *Nat. Mater.* **2013**, *12*, 1137–1143.
[58] K. Dong, J. Liang, Y. Wang, Z. Xu, Q. Liu, Y. Luo, T. Li, L. Li, X. Shi, A. M. Asiri, Q. Li, D. Ma, X. Sun, *Angew. Chem. Int. Ed.* **2021**, *60*, 10583–10587.
[59] Z. Xu, J. Liang, Y. Wang, K. Dong, X. Shi, Q. Liu, Y. Luo, T. Li, Y. Jia, A. M. Asiri, Z. Feng, Y. Wang, D. Ma, X. Sun, *ACS Appl. Mater. Interfaces* **2021**, *13*, 33182–33187.
[60] X. Zhao, Y. Wang, Y. Da, X. Wang, T. Wang, M. Xu, X. He, W. Zhou, Y. Li, J. N. Coleman, Y. Li, *Natl. Sci. Rev.* **2020**, *7*, 1360–1366.
[61] M. T. M. Koper, *J. Electroanal. Chem.* **2011**, *660*, 254–260.
[62] A. Kulkarni, S. Siahrostami, A. Patel, J. K. Nørskov, *Chem. Rev.* **2018**, *118*, 2302–2312.
[63] J. K. Nørskov, J. Rossmeisl, A. Logadottir, L. Lindqvist, J. R. Kitchin, T. Bligaard, H. Jónsson, *J. Phys. Chem. B* **2004**, *108*, 17886–17892.
[64] J. Gao, H. bin Yang, X. Huang, S.-F. Hung, W. Cai, C. Jia, S. Miao, H. M. Chen, X. Yang, Y. Huang, T. Zhang, B. Liu, *Chem* **2020**, *6*, 658–674.
[65] S. Stoll, A. Schweiger, *J. Magn. Reson.* **2006**, *178*, 42–55.
[66] T. M. Casey, "cwEPR," can be found under https://nl.mathworks.com/matlabcentral/fileexchange/73292-cwepr**2020**.
[67] TURBOMOLE, Version 7.5, *TURBOMOLE Gmbh, Karlsruhe, Germany* **2020**.
[68] J. Baker, *J. Comput. Chem.* **1986**, *7*, 385–395.
[69] P. H. M. Budzelaar, *J. Comput. Chem.* **2007**, *28*, 2226–2236.
[70] J. P. Perdew, K. Burke, M. Ernzerhof, *Phys. Rev. Lett.* **1996**, *77*, 3865–3868.
[71] F. Weigend, R. Ahlrichs, *Phys. Chem. Chem. Phys.* **2005**, *7*, 3297–3305.
[72] F. Weigend, M. Häser, H. Patzelt, R. Ahlrichs, *Chem. Phys. Lett.* **1998**, *294*, 143–152.
[73] S. Grimme, J. Antony, S. Ehrlich, H. Krieg, *J. Chem. Phys.* **2010**, *132*, 154104.
[74] Z. Liang, H.-Y. Wang, H. Zheng, W. Zhang, R. Cao, *Chem. Soc. Rev.* **2021**, *50*, 2540–2581.
[75] M. Zhou, L. A. Wolzak, Z. Li, F. J. de Zwart, S. Mathew, B. de Bruin, *J. Am. Chem. Soc.* **2021**, *143*, 20501–20512.
[76] N. P. Van Leest, M. A. Tepaske, B. Venderbosch, J.-P. H. Oudsen, M. Tromp, J. I. Van Der Vlugt, B. De Bruin, *ACS Catal.* **2020**, *10*, 7449–7463.
[77] P. W. Atkins, L. Jones, *Chemical Principles: The Quest for Insight*, W. H. Freeman **1999**.
[78] I. Martínez, *Termodinámica Básica y Aplicada*, Ed. Dossat **1992**.
[79] "Computational Chemistry Comparison and Benchmark Database," can be found under http://cccbdb.nist.gov/.

Manuscript received: June 13, 2023
Revised manuscript received: July 12, 2023
Accepted manuscript online: July 20, 2023
Version of record online: ■■, ■■

RESEARCH ARTICLE

Connect them: A bottom-up approach is applied to construct a conjugated C–C bond between the commercial Vulcan carbon electrode and an organometallic catalyst. The strong electrode/active site interaction enables superior and selective oxygen reduction reaction to hydrogen peroxide in neutral media.

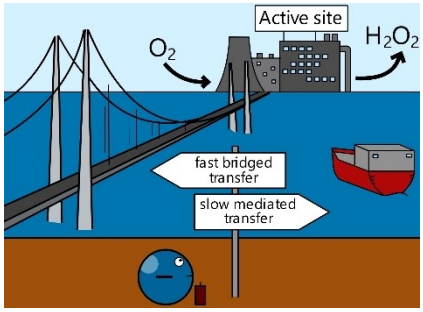

Dr. J. Biemolt, E. J. Meeus, F. J. de Zwart, J. de Graaf, P. C. M. Laan, Prof. Dr. B. de Bruin, Dr. T. Burdyny, Prof. Dr. G. Rothenberg, Prof. Dr. N. Yan**